Tribology International 123 (2018) 216–223

Contents lists available at ScienceDirect

Tribology International

journal homepage: www.elsevier.com/locate/triboint

Multi-objective optimization on dimple shapes for gas face seals

Xiuying Wang[a], Liping Shi[a,b], Qinwen Dai[a], Wei Huang[a], Xiaolei Wang[a,*]

[a] College of Mechanical and Electrical Engineering, Nanjing University of Aeronautics and Astronautics, Nanjing, China
[b] School of Mechanical Engineering, Anhui University of Technology, Ma'anshan, China

ARTICLE INFO

Keywords:
Surface texture
Face seals
Shape optimization
Multi-objective optimization

ABSTRACT

The shape of surface texture has a significant effect on the performance of face seals. Many studies found that the textures designed for improving load carrying capacity tend to increase leakage at the same time. Therefore, a multi-objective optimization approach is presented to optimize the dimple shapes with freedom edges. It has been found the dimples with asymmetric "V" shape offer better performance in terms of load carrying capacity and leakage. Moreover, the optimal shapes are compared with four kinds of optimal regular shapes under different rotating speeds. The results show that the superiority of shape optimization is more obvious in conditions with high speed.

1. Introduction

There is an increasing demand for reliable and durable face seals with low leakage and low friction under high speed, high temperature, and complex working conditions. Surface texturing has been proven to be an effective means to improve the tribological performance of sliding surfaces because of the hydrodynamic effect under full or mixed lubrication and lubricant reservoir effect under staved lubrication conditions [1–5].

The patterns of grooves and dimples are common types of surface texture for face seals [1–15]. They are typical representatives of connected texture and disconnected texture, respectively. Grooves such as spiral grooves [10–13] and T-shape grooves [9] have been widely used in face seals due to the pumping effect and hydrodynamic effect. Dimples were also proven to reduce friction or improve load carrying capacity under different conditions [3–7,14–18], meanwhile, they were expected to obtain a better hydrodynamic effect due to the disconnected structure [7,15]. Nakano et al. [7] found that cast iron surfaces with dimples had lower friction than the surfaces with grooves or meshes under lubricated conditions. Shi et al. [14] found that elliptical dimples with a high area density can obtain a higher load carrying capacity and higher gas film stiffness than grooves for gas lubrication. With further research, dimple shape has become a hot factor in the optimization of surface textures. Lu and Khonsari [2] reported that bushing with elliptical dimples has a lower friction coefficient than that with circular dimples under mixed lubrication. Uddin et al. [19] found that square shape dimples with a single wedge-bottom profile offered better tribological performance than triangular, chevron, circular and elliptical shapes. In view of the above studies, a conclusion can be drawn that the dimple shape is an essential factor to improve the tribological performance. Therefore, beyond the above regular shapes, are there any other shapes of dimples which can provide a better impact on the performance of sliding surface? Shen and Khonsari [20,21] conducted numerical optimization for complex dimple shapes using a sequential quadratic programming (SQP) algorithm. The optimal shape which can produce the maximum load carrying capacity was obtained by changing the design variables from an arbitrary shape. This work provides a possibility for further optimization of texture shapes.

Leakage is another important factor for gas face seals. However, it is difficult to improve the load carrying capacity or opening force and simultaneously reduce the leakage through surface texturing [8,10,22]. The clearance of seal rings increases with the increasing opening force, which leads to an undesirable increase of leakage [8]. In order to ease the case, the seal with double-row spiral grooves was presented where one row can pump the leaked medium back to the sealed space. But such a seal tends to have a complicated structure, needs larger installation space and can only be applied under low pressure differences [8]. Moreover, the load carrying capacity and the leakage rate were analyzed independently in most of the studies. It is difficult to obtain a better combination performance objectively by a single objective analysis.

This study aims to provide a multi-objective optimization approach specially for conflicting objectives i.e., load carrying capacity and leakage rate, to optimize the shape of dimples on gas face seals. The models of dimples and multi-objective optimization problem are established where the dimples have an arbitrary shape on a certain

* Corresponding author.
E-mail address: wxl@nuaa.edu.cn (X. Wang).

https://doi.org/10.1016/j.triboint.2018.03.011
Received 24 July 2017; Received in revised form 9 March 2018; Accepted 13 March 2018
Available online 15 March 2018
0301-679X/

Nomenclature

h	gas film thickness
F_t	non-dominated front
h_0	sealing clearance
M	average molar mass of gas
h_g	groove depth
P_0	initial population
l	inner diameter of dimple region of type a
P_t	population at N_{th} iteration
m	number of design variables
Q	leakage rate
n_r	rotating speed
Q_t	population obtained by crossover and mutation
p	gas film pressure
R	gas constant
p_a	atmospheric pressure
R_t	union of P_t and Q_t
r	coordinate in the radial direction
T	thermodynamic temperature
r_I	inner diameter of sealing ring
ω	angular velocity
r_O	outer diameter of sealing ring
W	load carrying capacity
α	small angle of dimple region of type b
$\overline{R}$	dimensionless coordinate in the radial direction
β	large angle of dimple region of type b
$\overline{\vartheta}$	dimensionless coordinate in the circumferential direction
Θ	coordinate in the circumferential direction
$\overline{H}$	dimensionless gas film thickness
γ	gas pressure to density ratio
$\overline{P}$	dimensionless gas film pressure
δ	angle of computing domain
$\overline{Q}$	dimensionless leakage rate
ρ	gas density
$\overline{W}$	dimensionless load carrying capacity
μ	dynamic viscosity of gas
NSGA-II	elitist non-dominated sorting genetic algorithm

constraint. Then, the optimal dimple shapes and the Pareto-optimal sets are obtained using the elitist non-dominated sorting genetic algorithm (NSGA-II). Furthermore, the optimal shapes are compared with the optimal regular shapes, including circle, ellipse, square and triangle, under different rotating speeds.

2. Optimization method

2.1. Physical model and governing equation

The face seal is composed of two sealing rings. Fig. 1 shows the physical model, where r_I and r_O are the inner radius and outer radius of the rings, respectively. The sealing faces are separated by a layer of gas film with the thickness of h_0. n_r is the rotating speed, and h_g is the depth of dimples. In this study, 24 dimples are uniformly distributed on the stationary ring face. A sector unit cell containing one dimple is considered as the computing domain, and δ is the angle of computational domain.

In order to optimize the shape of the dimple from arbitrary geometry, there are 2n control points for one dimple which is formed by connecting the adjacent points. In this study, the shapes of dimples include two types: type a and type b, as shown in Fig. 2. For type a, the control points of n-i^{th} and $2n$-i^{th} (i = 0,1, …n-1) are located at the same radius, and they are free in the circumferential direction under a certain constraint which is shown in the multi-objective optimization model. The coordinates of these points are shown in Table 1. Based on this principle, 2n + 2 design variables are required, and they are θ_1, θ_2, …θ_n, θ_1^a, θ_2^a, …θ_n^a, l, L. For type b, the regularity is similar to that of type a, but the points of n-i^{th} and $2n$-i^{th} (i = 0,1, …n-1) are located at the same angle and they are free in the radial direction.

The number of design variables $m = 2n+2$ is an important factor for the computing accuracy and efficiency. Generally, the more the design variables, the smoother the edges of optimal shapes, however, the longer the computing time. Take type a as an example, the number of design variables m is studied in this study. It is found that when m is increased from 8 to 16, the optimal shapes have similar geometries and the edges become smoother and smoother, meanwhile, the computing times increase at an increasing rate. For m = 14, the optimized shapes have relatively smooth edges, and the computing time is 247 h which is 32% smaller than the computing time (367 h) of m = 16. Based on the computing time and shape accuracy, m = 14 is chosen in this study.

The two-dimensional steady-state Reynolds equation in the polar coordinates is employed to analyze the gas film pressure distribution p (r,θ). The equation can be expressed as:

$$\frac{\partial}{\partial r}\left(\frac{\rho r h^3}{\mu}\frac{\partial p}{\partial r}\right)+\frac{1}{r}\frac{\partial}{\partial \theta}\left(\frac{\rho h^3}{\mu}\frac{\partial p}{\partial \theta}\right)=6\omega r\frac{\partial(\rho h)}{\partial \theta} \tag{1}$$

where r and θ are the polar coordinates in the radial and circumferential directions, respectively; μ is the dynamic viscosity of gas, which is assumed as a constant in this study; ρ is the gas density; p is the gas pressure; h is the gas film thickness which is equal to h_0+h_g in the dimple region and equal to h_0 beyond the dimple region; and ω is the angular velocity which is equal to $2\pi n_r/60$.

Reynolds number, defined as $Re = \frac{\rho v h}{\mu}$ where v is the peripheral velocity of the seal face, is a dimensionless number that characterizes the state of fluid. Generally, the flow can be treated as laminar when Re < 1000 [23]. In this study, an example with the rotating speed of 10000 rpm is mainly studied, where the maximum Re is not more than 350, so laminar flow is assumed in this model.

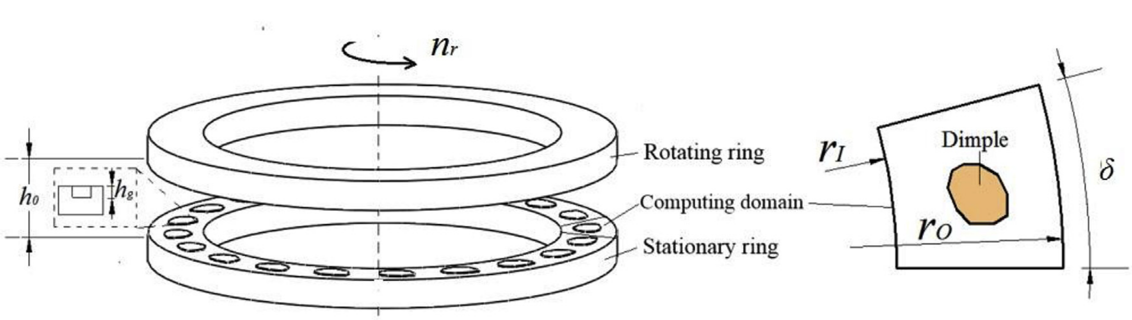

Fig. 1. Physical model of the face seal.

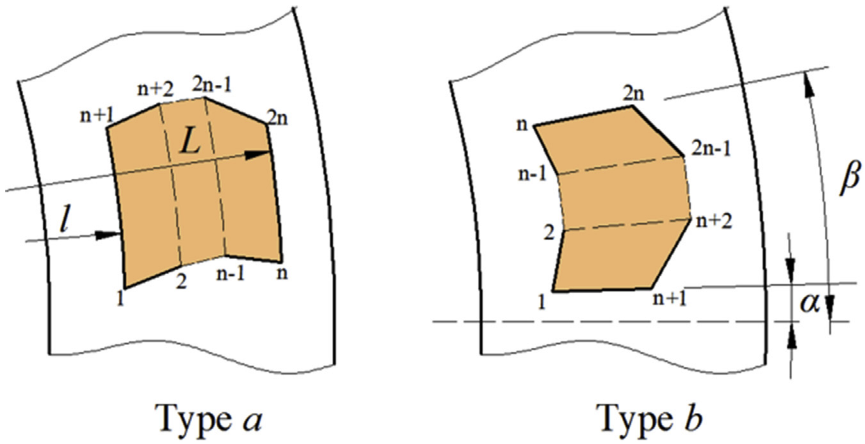

Fig. 2. Geometrical models of dimples in polar coordinate.

Table 1
Coordinates of the points in the physical model of dimples.

	Points	i (i = 1,2 … …n)	j (j = n+1,n+2 … …2n)
Coordinates	Type a ($dr=(L\text{-}l)/(n\text{-}1)$)	($l + dr \times (i\text{-}1)$, θ_i)	($l + dr \times (j\text{-}n\text{-}1)$, $\theta_{j\text{-}n}+\theta^a_{j\text{-}n}$)
	Type b ($d\theta=(\beta\text{-}\alpha)/(n\text{-}1)$)	(r_i, $\alpha+d\theta \times (i\text{-}1)$)	($r_{j\text{-}n} + r^b_{j\text{-}n}$, $\alpha+d\theta \times (j\text{-}n\text{-}1)$)

It is assumed that the sealing gas is of uniform temperature, because the friction of non-contact gas seals is quite small and the temperature rises slowly. Moreover, it is considered as an ideal gas. The ideal gas state equation is written as:

$$\frac{p}{\rho} = \frac{RT}{M} = \gamma \tag{2}$$

where M is the average molar mass of gas, equal to 29 g/mol; R is the gas constant, equal to 8.314 cm^3 MPa/mol·K; T is the absolute temperature of the sealing system and is taken as 300 K in this study. The ratio of p and ρ is defined as γ and will be used in the calculation of the leakage rate.

The pressures at the outer radius and inner radius are set to p_I and p_O, respectively, and the periodic boundary condition is applied in the circumferential directions to account for the interaction between dimples. The boundary condition is written as:

$$\begin{cases} p(r=r_I,\theta)=p_I \\ p(r=r_O,\theta)=p_O \\ p(r,\theta=0)=p(r,\theta=\delta) \\ \frac{\partial p}{\partial\theta}(r,\theta=0)=\frac{\partial p}{\partial\theta}(r,\theta=\delta) \end{cases} \tag{3}$$

The performance parameters, including load carrying capacity W and leakage rate Q, are expressed as:

$$W=\int_0^\delta\int_{r_I}^{r_O} p(r,\theta)rdrd\theta \tag{4}$$

$$Q=-\int_0^\delta\left(\frac{prh^3}{12\mu\gamma}\frac{\partial p}{\partial r}\right)_{r=r_I}d\theta \tag{5}$$

The load carrying capacity W is the integral of the gas film pressure across the entire computing domain. The leakage rate Q is the flow rate in the radial direction and it follows the flow continuity principle. It could be calculated no matter which radius is chosen. So the inner radius is adopted in the following evaluation.

The equations and performance parameters are nondimensionalized based on the dimensionless terms:

$$\overline{R}=\frac{r}{r_I},\ \overline{H}=\frac{h}{h_0},\ \overline{P}=\frac{p}{p_a},\ \overline{W}=\frac{W}{p_a r_I^2},\ \overline{Q}=\frac{12Q\mu\gamma}{p_a^2 h_0^3} \tag{6}$$

The dimensionless Reynolds equation can be expressed as:

$$\frac{1}{\overline{R}}\frac{\partial}{\partial\overline{R}}\left(\overline{R}\overline{P}\overline{H}^3\frac{\partial\overline{P}}{\partial\overline{R}}\right)+\frac{1}{\overline{R}^2}\frac{\partial}{\partial\theta}\left(\overline{P}\overline{H}^3\frac{\partial\overline{P}}{\partial\theta}\right)=\Lambda\frac{\partial(\overline{P}\overline{H})}{\partial\theta} \tag{7}$$

where $\Lambda=\frac{6\mu\omega r_I^2}{p_a h_0^2}$ is the compressibility number.

The successive over relaxation (SOR) method is utilized to solve the dimensionless Reynolds equations. The dimensionless performance parameters are obtained according to Eq. (4), Eq. (5) and Eq. (6).

2.2. Multi-objective optimization model

For a multi-objective optimization problem, usually there is not a single optimal solution but an optimal set called as Pareto-optimal set. The element in Pareto-optimal set is called as Pareto-optimal solution which means that one objective is the best when other objectives are fixed. In other words, it is impossible to make one of the objectives better than the optimal solution without destroying any other objectives. The multi-objective optimization model can be expressed as:

$$\min f(x) = [f_1(x), f_2(x), \cdots, f_m(x)] \text{ subject to } (s.t.)\ x \text{ meets certain constraints} \tag{8}$$

where $f_1(x)$, $f_2(x)$, …, $f_m(x)$ are the objective functions, and x is a vector formed by independent variables.

In this study, the dimensionless load carrying capacity $\overline{W}$ and the dimensionless leakage rate $\overline{Q}$ are the objectives, and the dimensionless design variables related to the dimple shapes are the independent variables. Because the minimum values of objective functions are the goal of the multi-objective optimization, $-\overline{W}$ is taken as an objective according to the practical meaning of $\overline{W}$. The model of multi-objective optimization for dimples of type a is expressed as:

$$\begin{aligned} &\min\ [-\overline{W}(x_a), \overline{Q}(x_a)] \\ &\text{where } x_a=[\theta_1,\theta_2,\cdots,\theta_{n-1},\theta_n,\theta_1^a,\theta_2^a,\cdots,\theta_{n-1}^a,\theta_n^a, l/r_I, L/r_I] \\ &s.t.\ \ r_I\le l<L\le r_O,\ \ 0\le\theta_i\le\delta, 0\le\theta_i^a\le\delta, \\ &0\le\theta_i+\theta_i^a\le\delta\ \ (i=1,2,\cdots,n) \end{aligned} \tag{9}$$

where x_a is a vector formed by the dimensionless parameters of dimples of type a.

Similarly, the model of multi-objective optimization for dimples of type b is expressed as:

$$\min\ [-\overline{W}(x_b),\ \overline{Q}(x_b)]$$
$$\text{where } x_b = [\bar{r}_1,\ \bar{r}_2, \cdots, \bar{r}_{n-1},\ \bar{r}_n,\ \bar{r}_1^b,\ \bar{r}_2^b, \cdots, \bar{r}_{n-1}^b,\ \bar{r}_n^b,\ \alpha,\ \beta]$$
$$s.\ t.\quad 0 \le \alpha < \beta \le \delta,\quad 1 \le \bar{r}_i \le r_O/r_I,\quad 1 \le \bar{r}_i^b \le r_O/r_I,$$
$$1 \le \bar{r}_i + \bar{r}_i^b \le r_O/r_I\ \ (i = 1,2,\cdots,n) \tag{10}$$

where $\bar{r}_i = r_i/r_I$, $\bar{r}_i^b = r_i^b/r_I$ $(i = 1,2,\cdots,n)$, and x_b is a vector formed by the dimensionless parameters of dimples of type b.

The multi-objective optimization problem is solved using the elitist non-dominated sorting genetic algorithm (NSGA-II). The algorithm brings forward a fast non-dominate sorting approach; and its computing complexity is reduced greatly [24,25]. Fig. 3 presents a flowchart of NSGA-II. The optimal results are obtained through repeated iteration. Staring from a random population P_0, a new population Q_t is obtained by genetic manipulation for the population P_t, then, a non-dominated front F_t is formed by sorting and selecting for the union set R_t of P_t and Q_t. The population P_{t+1} is formed by individuals in R_t corresponding to the top N individuals in F_t, where N is the population size. The work repeats until the termination condition that the population distance of adjacent iterations is less than 10^{-5} is satisfied.

The values of geometric parameters and condition parameters used in this study are shown in Table 2.

3. Results and discussion

3.1. Shape optimization results

The multi-objective optimization problem is solved using NSGA-II according to the flowchart in Fig. 3. The Pareto-optimal sets and optimal objectives for type a and type b are obtained, respectively. The number of solutions in Pareto-optimal set is related to the population size and Pareto fraction. Too many solutions are unnecessary because they are continuous and the adjacent solutions have high similarities. So it is set to 7 in order to show the optimal shapes clearly.

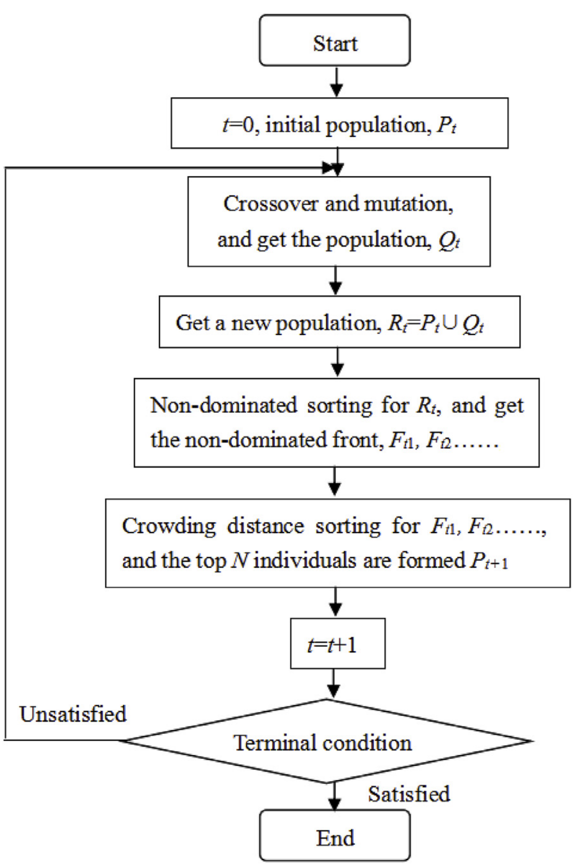

Fig. 3. Flowchart of the NSGA-II.

Table 2
Geometric parameters and condition parameters.

Items	Values
Inner radius of computing domain r_I, mm	17.9
Outer radius of computing domain r_O, mm	23.4
Angle of computing domain ω	π/12
Depth of dimples h_g, μm	10
Gap of two specimen h_0, μm	10
Sealed gas dynamic viscosity μ, MPa·s	18.448×10^{-12}
Atmospheric pressure p_a, MPa	0.101
Boundary pressure of inner side p_I, MPa	0.202
Boundary pressure of outer side p_O, MPa	0.101
Rotating speed n_r, rpm	3000, 10000, 20000

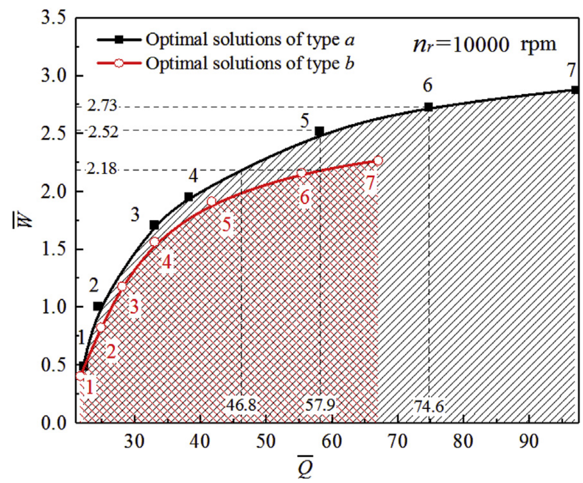

Fig. 4. The optimal solutions of multi-objective optimization.

Fig. 4 shows the solutions of the multi-objective optimization for type a and type b. The horizontal axis is the dimensionless leakage rate and the vertical axis is the dimensionless load carrying capacity. Take type a as an example, a curve is formed by connecting the optimal points, which divides the area into two parts. The optimal solutions are the boundary of the shadow area. For all dimple shapes of type a except optimal shapes, their dimensionless load carrying capacities and dimensionless leakage rates will fall into the black shadow area. Similar conclusion can be drawn for type b. As shown in Fig. 4, the growth rate of optimal dimensionless load carrying capacity is getting smaller as the optimal dimensionless leakage rate increases linearly. In other words, the optimal dimensionless leakage rate will increase sharply when the optimal dimensionless load carrying capacity increases slightly. That is to say, blindly pursuing the maximum load carrying capacity is not appropriate in the design of dimples for gas face seals because drastic rises may occur in the leakage rate.

As can also be observed in Fig. 4, the optimal dimensionless load carrying capacity of type b is smaller than that of type a under the same dimensionless leakage rate for all solutions, meanwhile, the optimal dimensionless leakage rate of type b is larger than that of type a under the same dimensionless load carrying capacity. For example, the optimal dimensionless load carrying capacity of type a is 2.52 when the dimensionless leakage rate is 57.9, higher than that of other type a with the same dimensionless leakage rate. It is 2.18 for type b, which is 13.5% lower than that of type a. Similarly, the optimal dimensionless leakage rate of type a can be as low as 46.8 when the dimensionless load carrying capacity is 2.18, and it is 57.9 for type b, which is 23.7% higher than that of type a. In view of this, the optimal shapes of type a can provide a better combination performance than that of type b. The reason may be that the freedom in the circumferential direction is beneficial to produce a larger load carrying capacity or a lower leakage

Table 3
Optimal shapes and dimensionless pressure distributions.

Solution order	1	2	3	4	5	6	7	Colorbar
Type *a*	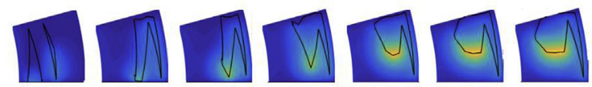							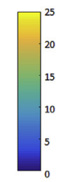
Type *b*	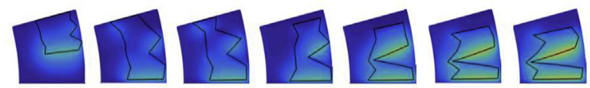							

Note: the black line is the profile of dimple and the contour is the dimensionless pressure distribution

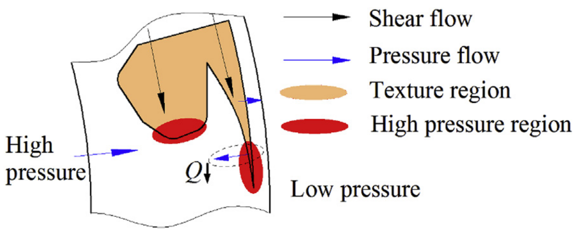

Fig. 5. Mechanism of optimal shape of type *a*.

rate, but it was constrained for the shape of type *b*.

Moreover, as can be seen in Fig. 4, the value spans of optimal objectives are wide. That is to say, the optimization results can provide a reference for a variety of leakage or load carrying capacity requirements, meanwhile, the objectives span of type *a* is larger than that of type *b*. For example, when the dimensionless leakage rate of 74.6 is allowed, the optimal solutions of type *b* can't provide a more effective reference for the design of dimples. The optimal shape of type *a* corresponding to the dimensionless load carrying capacity of 2.73 can be selected. In this way, the dimples can satisfy the requirement of leakage rate and can generate a load carrying capacity as large as possible at the same time. Considering this view and the above analysis, the optimal shapes of type *a* are better than those of type *b*.

Table 3 shows the optimal dimple shapes and the dimensionless pressure distributions corresponding to the above solutions. The detailed values of the design variables are shown in Appendix. As shown in Table 3, the optimal shapes for type *a* have very similar geometries with asymmetric “V” apart from the solution 1. The widths and areas of edges near inner side are larger than those near outer side. As the solution order increases, the widths and areas of edges near inner side increase but the edges near outer side are almost same. It is hard to get such special optimal shapes through imagination or subjective designing. Numerical optimization may be the only way. As also can be seen in Table 3, the optimal shapes for type *b* are constrained greatly in the circumferential direction, their edges mainly show a jagged shape in the radial direction. But the trend in the radial direction is not a very effective factor according to the optimal solution in Fig. 4. In addition, for type *a* and type *b*, all of the optimal dimples are located at the outer side of sealing faces. The reason maybe that gas flows into the sealing clearance from inner side driven by the high pressure at inner radius, then the gas pressure decreases from inner to outer, and it is further enhanced by the dimples near outer side.

Moreover, as shown in Table 3, the dimensionless pressure distributions between type *a* and type *b* are different. For type *a*, high pressure is mainly generated at the end of wide edge, which is located in the middle of the computational domain. However, there are obvious breaks for the pressure distribution of optimal type *b*. In general, the optimal shapes of type *a* have a more uniform pressure distribution than those of type *b*, which may lead to a higher load carrying capacity. Meanwhile, for most optimal shapes of type *a,* the dimple areas are smaller than those of type *b*, which may lead to a lower leakage rate, because the untextured area is a critical factor for the leakage. In addition, there are two flows including pressure flow and shear flow in the computational domain for the optimal shape of type *a*, as shown in Fig. 5. High pressure is also generated at the end of the narrow edge, and the mediums will flow back to inner side driven by the pressure difference. So the leakage rate will be reduced to some extent.

3.2. Comparison with optimal regular shapes

3.2.1. Regular shapes

The optimal dimple shapes of type *a* are compared with optimal regular shapes including circle, ellipse, square and triangle. The design variables are determined according to their features. Table 4 shows the regular shapes and their design variables. Different constraints are applied to the design variables for different dimples to ensure that the dimples do not exceed the computational domain. For all of these dimples, their depths are equal to the dimple depths of type *a*. The optimal solutions are obtained using the same multi-objective optimization method.

Table 4
Models of regular shapes.

No.	Description	dimple shapes	Design variables	Number of design variables
1	Circle	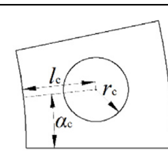	α_c, l_c, r_c	3
2	Ellipse	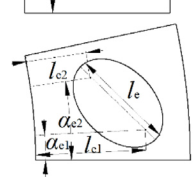	α_{e1}, l_{e1}, α_{e2}, l_{e2}, l_e	5
3	Square	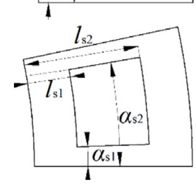	α_{s1}, l_{s1}, α_{s2}, l_{s2}	4
4	Triangle	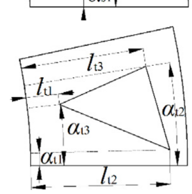	α_{t1}, l_{t1}, α_{t2}, l_{t2}, α_{t3}, l_{t3}	6

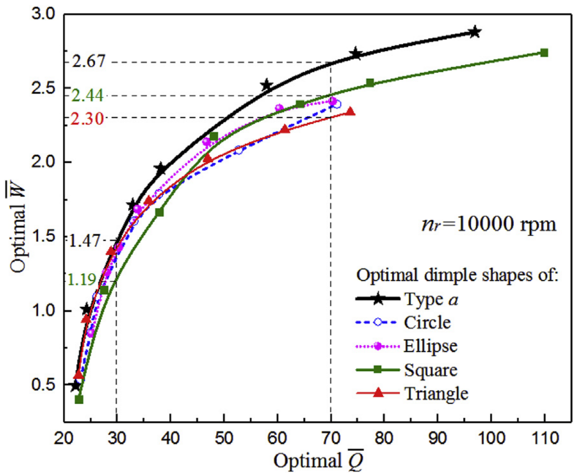

Fig. 6. Optimization results for different dimple shapes.

3.2.2. Optimal results for regular shapes

Fig. 6 shows optimal solutions of type a and regular shapes. Table 5 shows the corresponding optimal regular shapes and their dimensionless pressure distributions. Similar to Fig. 4, the growth rate of optimal dimensionless load carrying capacity is getting smaller as the optimal dimensionless leakage rate increases. In addition, for all shapes except optimal shapes, their dimensionless load carrying capacity and dimensionless leakage rate will fall below the optimal curves.

It can also be seen in Fig. 6 that the optimal dimensionless load carrying capacities of regular shapes are smaller than those of type a under the same leakage rate in most cases. That is to say, the optimal shapes of type a can offer better performance in comparison with other optimal regular shapes. For example, the optimal shape of type a has the dimensionless load carrying capacities of 1.47 and 2.67 when the dimensionless leakage rates are 30 and 70, which is 23.5% and 16.1% higher than the lowest values of 1.19 and 2.30, respectively. Meanwhile, the optimal shape of square has the second largest optimal dimensionless load carrying capacity 2.44 when the dimensionless leakage rate is 70, but it has the lowest optimal dimensionless load carrying capacity 1.19 when the dimensionless leakage rate is 30. Generally speaking, the optimal shape of type a is the most satisfactory under both low and high leakage rate conditions, and the optimal square shape can be the second choice under a high leakage rate condition. Certainly, the optimal square shapes provide a slightly lower load carrying capacity than the optimal shapes of type a under the same leakage rate, but they have a lower design complexity.

The wide spans of optimal objectives mean that the optimization results can provide references for a variety of leakage or load carrying capacity requirements. In view of this, the optimal shapes of type a and optimal square shapes are more favorable than other optimal shapes, because they have larger spans.

As shown in Table 5, similar to the optimal shapes of type a, as the solution order increases, the areas of optimal regular shapes are becoming larger in general, and the locations of dimples move to the upstream and outer side. For the optimal square shapes, the increasing length in the radial direction plays an important role in preventing flow, improving film pressure and enlarging the leakage rate at the same time. The decreasing length in the circumferential direction can control the leakage rate to some extent. So the length-width ratio, defined as the ratio of the length in the circumferential direction to the length in the radial direction of the square dimple, is a sensitive factor for the pressure distribution.

In summary, the optimal shapes of type a are the most satisfactory. The optimal square shapes can be the second choice because of the large span of optimal solutions and the simple structures.

Table 5
Optimal regular shapes and dimensionless pressure distributions.

Solution order	1 2 3 4 5 6 7	Colorbar
Circle	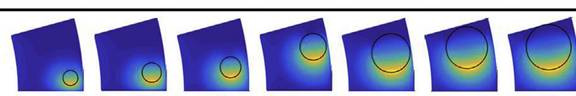	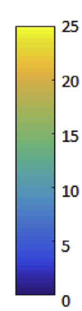
Ellipse	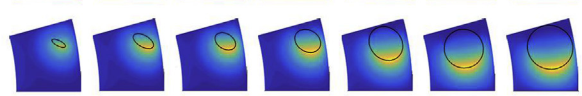	
Square	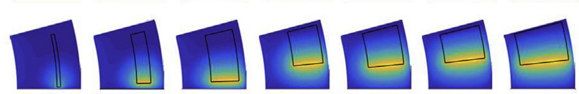	
Triangle	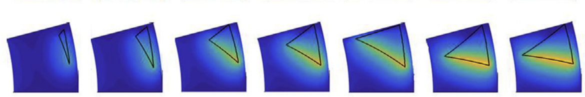	

Table 6
Optimal shapes of type a and dimensionless pressure distributions for n_r = 3000 rpm and n_r = 20000 rpm.

Solution order	1 2 3 4 5 6 7	Colorbar
n_r=3000rpm	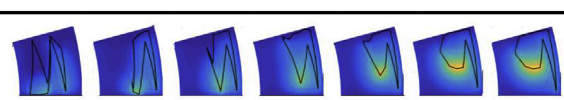	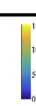
n_r=20000rpm	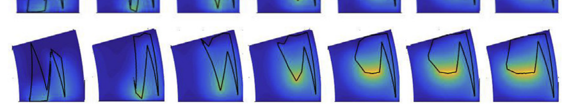	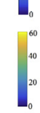

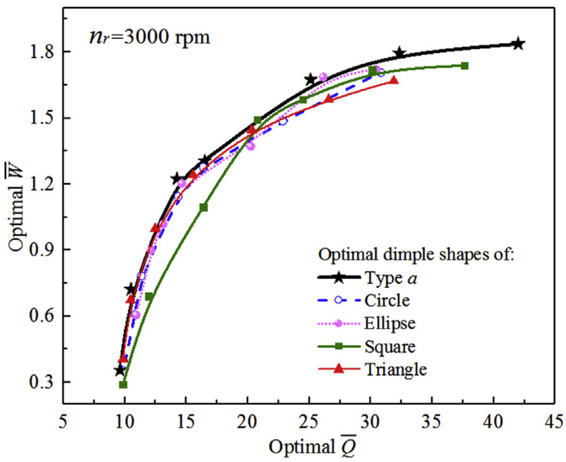

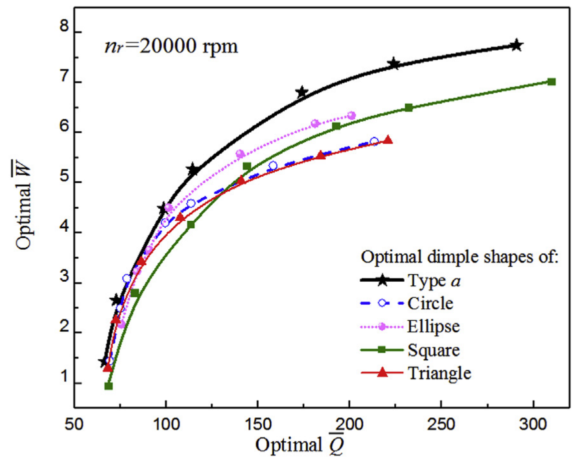

Fig. 7. Optimal solutions of different dimple shapes: (a) n_r = 3000 rpm, (b) n_r = 20000.

3.2.3. Results under different rotating speeds

In order to verify if the rotating speed has obvious influence on the optimal shapes, the same approach is carried out for a quite low speed n_r = 3000 rpm and a quite high speed n_r = 20000 rpm under the same laminar assumption, although the maximum Re is about 1675 for the speed of 20000 rpm, and turbulence flow should be considered in real case.

Table 6 shows the optimal dimple shapes of type a for n_r = 3000 rpm and n_r = 20000 rpm. Although there are small differences between the same order solutions for different speeds, in general, they are similar.

Fig. 7 shows the optimal solutions of different dimple shapes for n_r = 3000 rpm and n_r = 20000 rpm. The optimal shape of type a shows a higher dimensionless load carrying capacity than other optimal shapes under the same dimensionless leakage rate for both low speed and high speed. Similarly, it can get a lower dimensionless leakage rate than other shapes under the same dimensionless load carrying capacity. Meanwhile, the solution spans of optimal type a are larger than other shapes, which means a broad guidance on different leakage or load carrying capacity requirements. Moreover, as can be seen in Figs. 6 and 7, the differences of optimal solutions between optimal shape of type a and other optimal shapes increase with the increasing rotating speed. The advantage of optimal type a is more obvious at high rotating speed.

The specific samples show the effectiveness of the multi-objective optimization for the dimple shape, and other working conditions can also be analyzed using this method when the actual condition parameters are specified.

4. Conclusions

In this study, a multi-objective optimization approach is presented to optimize the dimple shape for gas face seals.

For any types of dimple shape, each optimal shape can get a highest load carrying capacity under a given leakage rate or a lowest leakage rate under a given load carrying capacity. The wide spans of solutions mean the results can provide a reference for a variety of leakage or load carrying capacity requirements.

The optimal shapes of asymmetric "V" always show a best impact on the performance of gas face seals. The advantage of shape optimization using multi-objective approach for gas face seals is more obvious at high speed conditions.

Acknowledgment

This paper is based on the research work supported by the National Natural Science Foundation of China (No. 51675268), the Fundamental Research Funds for the Central Universities (No. NZ2016106), the Funding of Jiangsu Innovation Program for Graduate Education (No. KYLX16_0326), the China Scholarship Council (No. 201706830065) and the Natural Science Research Fund of Higher Education of Anhui Province (No. KJ2016A093).

Appendix

Table A1
Detailed values of the optimal shapes of type a in Table 3

Solutions orders	1	2	3	4	5	6	7
θ_1	0.25909	0.25559	0.25192	0.23943	0.22239	0.18404	0.17701
θ_2	0.00159	0.00458	0.06449	0.15392	0.12496	0.12429	0.1204
θ_3	0.00193	0.00318	0.01687	0.05402	0.10313	0.11217	0.11474
θ_4	0.00083	0.12445	0.1197	0.11791	0.11008	0.11235	0.11432
θ_5	0.25886	0.22637	0.20278	0.19645	0.21226	0.21676	0.23036
θ_6	0.00158	0.00306	0.0138	0.02404	0.02054	0.02008	0.01266
$\theta_1{}^a$	0.00101	0.00147	0.00466	0.011	0.01633	0.0177	0.02308
$\theta_2{}^a$	0.00099	0.00721	0.01778	0.07536	0.12821	0.13002	0.1382
$\theta_3{}^a$	0.2361	0.24411	0.24036	0.19893	0.15361	0.15056	0.14794
$\theta_4{}^a$	0.0033	0.11499	0.12739	0.13742	0.14145	0.14516	0.14768

$\theta_5{}^a$	0.00124	0.01964	0.04189	0.06085	0.03942	0.03919	0.02787
$\theta_6{}^a$	0.13152	0.23424	0.23526	0.22722	0.23294	0.23543	0.23637
l/r_{I}	1.00469	1.12325	1.14479	1.13878	1.13001	1.10213	1.08318
L/r_{I}	1.17265	1.27475	1.27935	1.2817	1.2835	1.28419	1.28461

Table A2
Detailed values of the optimal shapes of type *b* in Table 3

Solution orders	1	2	3	4	5	6	7
$\bar{r}_1$	1.12845	1.12189	1.11975	1.10649	1.08297	1.07185	1.05829
$\bar{r}_2$	1.13475	1.14054	1.13789	1.13950	1.12098	1.11425	1.08403
$\bar{r}_3$	1.12169	1.12526	1.11519	1.13936	1.08934	1.06188	1.03061
$\bar{r}_4$	1.12183	1.12753	1.11779	1.14132	1.11337	1.10803	1.08977
$\bar{r}_5$	1.11898	1.11634	1.12299	1.16799	1.13916	1.13477	1.13377
$\bar{r}_6$	1.11198	1.07776	1.07559	1.15367	1.13768	1.09672	1.08345
$\bar{r}_1$	0.15832	0.16872	0.17237	0.19568	0.21298	0.21882	0.22547
$\bar{r}_2$	0.17237	0.16164	0.15569	0.16070	0.16944	0.18174	0.20927
$\bar{r}_3$	0.13401	0.10485	0.09326	0.05913	0.02294	0.02272	0.02267
$\bar{r}_4$	0.17471	0.16803	0.16546	0.16591	0.16960	0.17808	0.17517
$\bar{r}_5$	0.15231	0.12844	0.05070	0.09884	0.13852	0.15376	0.15622
$\bar{r}_6$	0.16883	0.13301	0.11488	0.13268	0.13934	0.17770	0.18006
α	0.11970	0.01260	0.01300	0.01041	0.01286	0.01480	0.01495
β	0.26018	0.25945	0.25893	0.23485	0.21948	0.20462	0.20174

References

[1] Suh MS, Chae YH, Kim SS, Hinoki T, Kohyama A. Effect of geometrical parameters in micro-grooved crosshatch pattern under lubricated sliding friction. Tribol Int 2010;43(8):1508–17.
[2] Lu X, Khonsari MM. An experimental investigation of dimple effect on the stribeck curve of journal bearings. Tribol Lett 2007;27(2):169–76.
[3] Yu H, Huang W, Wang X. Dimple patterns design for different circumstances. Lubric Sci 2013;25(2):67–78.
[4] Tala-Ighil N, Fillon M. A numerical investigation of both thermal and texturing surface effects on the journal bearings static characteristics. Tribol Int 2015;90:228–39.
[5] Dobrica MB, Fillon M, Pascovici MD, Cicone T. Optimizing surface texture for hydrodynamic lubricated contacts using a mass-conserving numerical approach. ARCHIVE Proc.Inst. Mech. Eng. J. Eng. Tribol. 2010;224(J8):737–50.
[6] Zhan J, Yang M. Investigation on dimples distribution angle in laser texturing of cylinder–piston ring system. Tribol Trans 2012;55(5):693–7.
[7] Nakano M, Korenaga A, Korenaga A, Miyake K, Murakami T, Ando Y, et al. Applying micro-texture to cast iron surfaces to reduce the friction coefficient under lubricated conditions. Tribol Lett 2007;28(2):131–7.
[8] Sun J, Ma C, Yu Q, Lu J, Zhou M, Zhou P. Numerical analysis on a new pump-out hydrodynamic mechanical seal. Tribol Int 2017;106:62–70.
[9] Ma C, Bai S, Peng X. Thermoelastohydrodynamic characteristics of T-grooves gas face seals. Int J Heat Mass Tran 2016;102:277–86.
[10] Zirkelback N. Parametric study of spiral groove gas face seals. Tribol Trans 2000;43(2):337–43.
[11] Lee AS, Kim CU. Lubrication characteristics of spiral groove liquid seals for use in the Carrier of a vane-type external LPG fuel pump. Int J Automot Technol 2011;12(2):233–41.
[12] Miller BA, Woodruff GW. Numerical formulation for the dynamic analysis of spiral-grooved gas face seals. J Tribol 2001;123(2):395–403.
[13] Person V, Tournerie B. A numerical study of the stable dynamic behavior of radial face seals with grooved faces. J Tribol 1997;119(3):507–13.
[14] Shi L, Wang X, Su X, Huang W, Wang X. Comparison of the load-carrying performance of mechanical gas seals textured with microgrooves and microdimples. J Tribol 2015;138(2):88–90.
[15] Nakano M, Miyake K, Korenaga A, Sasaki S, Ando Y. Tribological properties of patterned nife-covered si surfaces. Tribol Lett 2009;35(2):133–9.
[16] Ryk G, Kligerman Y, Etsion I. Experimental investigation of laser surface texturing for reciprocating automotive components. Tribol Trans 2002;45(4):444–9.
[17] Xiong D, Qin Y, Li J, Wan Y, Tyagi R. Tribological properties of PTFE/laser surface textured stainless steel under starved oil lubrication. Tribol Int 2015;82:305–10.
[18] Wang X, Kato K, Adachi K. Running-in effect on the load-carrying capacity of a water-lubricated SiC thrust bearing. Proc IME J J Eng Tribol 2005;219(2):117–24.
[19] Uddin MS, Ibatan T, Shankar S. Influence of surface texture shape, geometry and orientation on hydrodynamic lubrication performance of plane-to-plane slider surfaces. Lubric Sci 2016;29(3):153–81.
[20] Shen C, Khonsari MM. Numerical optimization of texture shape for parallel surfaces under unidirectional and bidirectional sliding. Tribol Int 2015;82:1–11.
[21] Shen C, Khonsari MM. Texture shape optimization for seal-like parallel surfaces: theory and experiment. Tribol Trans 2016;59:698–706.
[22] Faria MTC. An efficient finite element procedure for analysis of high-speed spiral groove gas face seals. J Tribol 2001;123(1):165–9.
[23] Bassani R, Piccigallo B. Hydrostatic lubrication. Elsevier; 1992.
[24] Deb K, Pratap A, Agarwal S, Meyarivan T. A fast and elitist multiobjective genetic algorithm: NSGA-II. IEEE Trans Evol Comput 2002;6(2):182–97.
[25] Li H, Zhang Q. Multiobjective optimization problems with complicated Pareto sets, MOEA/D and NSGA-II. IEEE Trans Dielectr Electr Insul 2009;13(2):284–302.